Highly Stable CsPbBr$_3$@MoS$_2$ Nanostructures: Synthesis and Optoelectronic Properties Towards Implementation into Solar Cells

Achiad Goldreich[a],¶, Jonathan Prilusky[a],¶, Neena Prasad[a], and Lena Yadgarov*[a]

[a]   Department of Chemical Engineering
       Ariel University
       Ariel, 4076414, Israel

* Corresponding author; E-mail: lenay@ariel.ac.il

¶ These authors contributed equally

Supporting information for this article is given via a link at the end of the document.

Abstract: Halide perovskites (HPs) have gained significant interest in the scientific and technological sectors due to their unique optical, catalytic, and electrical characteristics. However, the HPs are prone to decomposition when exposed to air, oxygen, or heat. The instability of HP materials limits their commercialization, prompting significant efforts to address and overcome these limitations. Meanwhile, the transition metal dichalcogenides, such as MoS$_2$, are chemically stable and offer versatile properties suitable for electronic, optical, and catalytic applications. The layered structure of MoS$_2$ allows for the development of protective coatings for other nanoparticles. In this study, we successfully synthesized a novel CsPbBr$_3$@MoS$_2$ core-shell nanostructure (CS-NS) by enveloping CsPbBr$_3$ within a MoS$_2$ shell for the first time. We also demonstrate a significant enhancement in the stability of CS-NSs when dispersed in polar solvents for extended periods. Remarkably, the hybrid CS-NSs exhibits an absorption spectrum closely aligned with MoS$_2$ and photoluminescence (PL) quenching, indicating the potential for charge or energy transfer. We used finite difference time domain (FDTD) simulations to evaluate the efficiency of CS-NS-based solar cells and their potential for performance enhancement. This groundbreaking CS-NSs represents a significant advancement in harnessing halide perovskite materials for applications in photovoltaics and various optoelectronic devices.

Introduction

The ability to convert solar energy into efficient and environmentally friendly energy sources holds worldwide significance in both scientific and technological domains. Solar cells play a pivotal role in switching to sustainable energy alternatives by harvesting solar and converting it into useful power.[1] Over the past decade, halide perovskites (HPs) have emerged as one of the most promising semiconductors for photovoltaic solar cells due to their strong optical absorption, high carrier mobility, weak exciton binding energy, and low processing costs.[2] Also, HPs, in their bulk and nanocrystal form, exhibit excellent optoelectronic properties[3] and possess significant potential for applications including solar cells, light-emitting diodes (LEDs)[4] lasers,[5] photodetectors,[6] and photocatalysis.[7] HPs are typically formulated as ABX$_3$, where A is an organic or inorganic cation, B is a divalent metal ion (Pb^{2+} or Sn^{2+}), and X denotes a halogen element.

Significantly, CsPbBr$_3$ nanocrystals (NCs) have attracted considerable attention in research within the realm of all-inorganic HPs owing to their exceptional optical properties and strong light-matter interaction.[8] These NCs are potential candidates in several applications, such as liquid crystal displays, solar concentrators, and radiation detectors.[9] However, the inherent weak stability of the HPs presents a significant challenge for its practical implementation in devices.[10] The instability of the HPs NCs–is due to three main aspects: (1) the high ionicity of the bonding, which makes them unstable in any polar solvent; (2) moderate thermal stability due to low melting points of ~400°C; and (3) the dynamic nature of the ligand binding result in Ostwald ripening and a loss of structural and colloidal stability.[11]

The primary synthetic strategies for enhancing the stability of HPs NCs include using branched ligands or a core-shell architecture.[12] However, the branched capping ligands only partially stabilize the NCs when exposed to polar solvents or at elevated temperatures.[13] Hence, producing core-shell structures is preferred for colloidal semiconductor HPs NCs. The shell acts as a physical barrier that mitigates the presence of a surface trap, reduces exciton recombination, and enhances charge transfer.[14] This enrichment enhances the optical properties of the core, thereby improving the photovoltaic and photocatalytic properties.[14-15] Typically, the shell consists of SiO$_x$, metal oxides, or polymers.[16] When polymers are employed, the post-synthetic stabilization of HP NCs results in composite structures rather than the "classical" core-shell architecture.[16a] Namely, the polymers serve as a protective medium rather than a well-defined shell, leading to the poor dispersion of the NCs. SiO$_2$-encapsulated HPs NCs have been extensively explored and exhibit excellent stability and dispersibility in most media.[17] However, the SiO$_2$ shell often possesses significant thickness, impeding effective charge transfer and posing challenges to the applications of HPs NCs in the field of renewable energy.[18]

Another viable approach for creating stable core-shell NCs involves using metal chalcogenide shells such as PbS, CdS, and ZnS.[19] The use of inorganic shells allows the adjustment of the optoelectronic properties of the NCs and contributes to the

stabilization and passivation of the NCs.[20] However, it is worth noting that achieving a well-formed shell is a complex process, and often, only partial capping is performed, necessitating the continued use of ligands. An additional drawback of the all-inorganic passivation of the HPs-NCs can be the thickness of the shell.[6a, 21] A thick shell blocks charge extraction, increases lattice strain and reduces device performance.[21] An optimum shell thickness and composition should be carefully designed, and the corresponding influence on the optical properties needs to be inspected.

Given the outstanding chemical stability, exceptional optoelectronic properties, and other characteristics, including its size-dependent bandgap transitional metal di-chalcogenides (TMDs) emerge as excellent candidates.[22] Earlier studies have demonstrated that TMDs, like MoS_2, have great potential as surface passivation agents[23] and have shown great promise in various applications.[24] For instance, MoS_2 exhibits a bandgap in the visible range and features abundant active hydrogen sites at its edges provided by unsaturated sulfur species.[25] With properties such as visible band-edge excitation, metal-centered d–d transition,[26] and chemical inertness,[27] MoS_2 is well-suited for applications in solar cells, photodegradation of toxic materials, photovoltaics, and various electronic devices.[28] In solar cells, MoS_2 serves as an additive that remarkably stabilizes devices,[29] preventing the formation of shunt contacts[30] and acting as a hole-transport layer.[31] Additionally, these devices demonstrate ultrafast charge extraction at the interface.[32] Notably, MoS_2 surpasses $CsPbBr_3$ in terms of light absorption properties. Hence, the synergistic combination of $CsPbBr_3$ NCs with MoS_2 is anticipated to enhance the stability of NCs and lead to a notable improvement in their optical properties.[33] Conversely, hybrids and heterojunctions exhibit a partial interaction, resulting in properties similar to the superposition of their constituent materials.[34] $CsPbBr_3/MoS_2$ hybrid NSs are expected to be an excellent candidate for optoelectronic applications.[35] Although studies on $CsPbBr_3/MoS_2$ heterojunction have been conducted,[36] a core-shell system of these materials has not been investigated so far due to the absence of powerful and convenient synthetic approaches.

Here, we are developing an effective and novel synthetic method for $CsPbBr_3@MoS_2$ CS-NSs for the first time. Initially, we synthesized the $CsPbBr_3$ NCs via the hot injection method.[37] We synthesized the CS-NSs using pre-synthesized $CsPbBr_3$ NCs and $(NH_4)_2MoS_4$ precursor. The final structure is formed through a ligand exchange process and two-step annealing. Our study investigates the morphology and optical properties of the intermediate structures of CS-NSs to understand their formation mechanism. Despite the perceived simplicity of creating $CsPbBr_3@MoS_2$, we encountered significant challenges, including high orthogonal solubility and melting temperature of $CsPbBr_3$ vs MoS_2. Further, through theoretical finite difference time domain (FDTD) simulations, we determined the optimal core size and the ideal number of MoS_2 shell layers. This approach reduces the difficulties associated with experimental work, minimizing time consumption and resource-intensive efforts in the

laboratory. Also, the theoretical simulations offer a thorough examination and evaluation of the efficiency of CS-NS-based solar cells, providing valuable insights into the performance in photovoltaic applications.

Results and Discussion

Structural And Morphological Analysis

Figures 1 a and b represent the transmission electron microscope (TEM) images of the synthesized $CsPbBr_3$ NCs and $CsPbBr_3@MoS_2$ CS-NSs, illustrating the successful formation of the CS-NSs. The detailed description of the synthetic procedure is given in supporting information (SI) and illustrated in **Figures S1 and S2**. Briefly, the $CsPbBr_3$ NCs were synthesized using the hot injection method [37], and the MoS_2 shell was formed through the ligand-exchange process, followed by annealing at 500°C. The schematic representation of the MoS_2 shell formation over the $CsPbBr_3$ core is depicted in **Scheme 1**.
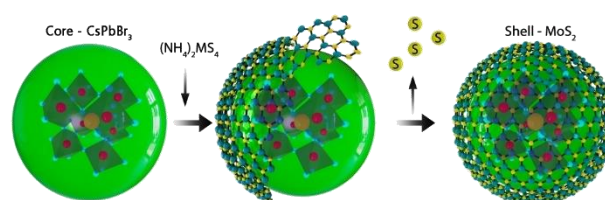
Scheme 1. Schematic representation of the Illustration of the MoS_2 shell over $CsPbBr_3$ and the forming of the $CsPbBr_3@MoS_2$ core-shell nanostructure synthesis

The highly crystalline nature of $CsPbBr_3$ NCs is evident in the TEM images, as represented in **Figures 1 a and S3 a**. The average particle size of these NCs is determined to be ~8±2 nm, and the particle size distribution graph is shown in **Figure S3 b**. Also, the spacing of the lattice fringes of the NCs was found to be 0.42 nm, corresponding to the (110) crystallographic planes of orthorhombic $CsPbBr_3$ NCs (**Figure S3 c**). Notably, this observation aligns with the obtained X-ray diffraction (XRD) pattern of $CsPbBr_3$ NCs (**Figure S4 a**).

The process of synthesizing CS-NSs involves first synthesizing $CsPbBr_3$ NCs, followed by a two-step annealing procedure. The TEM images of the partial formation of the MoS_2 shell over the $CsPbBr_3$ NCs at the first annealing step are shown in **Figures S5 a-d**. The final synthetic step includes the formation of CS-NSs by a complete sheathing $CsPbBr_3$ NCs by MoS_2 shell. The average radius of CS-NSs was 33.86±1.2 nm from the size distribution graph shown in **Figure S6 f**. The increase in the average radius of the $CsPbBr_3$ core is likely attributed to the Ostwald ripening effect, which occurred during the prolonged stirring period and ligand exchange.[38] The typical number of encapsulating MoS_2 layers ranges from 1 to 4 (**Figure 1 b and S5 a-d**). Notably, the synthetic process yields about 25% of the CS-NSs, with the remaining NSs being a hybrid configuration (**Figure S6**). Namely, we create a composite (hybrid) by blending $CsPbBr_3$ NCs with MoS_2 sheets that form during the synthesis process. A close TEM analysis shows that the core of $CsPbBr_3$ NCs did not fill the entire volume inside the MoS_2 shell, possibly due to lattice mismatch.[39]

According to the TEM micrographs presented in **Figure 1 c**, the lattice fringe spacings of 0.419 and 0.624 nm correspond to (110) and (002) crystallographic planes of $CsPbBr_3$ and MoS_2, respectively. Moreover, the selected area electron diffraction (SAED) image presents diffraction rings that match $CsPbBr_3$ NCs (green rings) and MoS_2 (azure rings, **Figure 1 d**). **Figure 1 e** shows the XRD patterns of $CsPbBr_3$, MoS_2, and the CS-NSs, which confirms the presence of $CsPbBr_3$ and MoS_2 phases in the $CsPbBr_3@MoS_2$ sample. The observed peaks in the XRD pattern closely align with the literature values for the crystallographic planes (112) and (002) of orthorhombic $CsPbBr_3$[40] (**Figure S4 a**) and the trigonal (2H) phase of MoS_2[41] (**Figure S4 b**). The EDS analysis provides the chemical composition of the CS-NSs and validates the presence of the constituent elements of $CsPbBr_3@MoS_2$ (**Figure S7**). However, the exact estimation of the Mo/S ratio is impossible due to the overlap between Mo, S, and Pb peaks.[42] The structural analysis done by TEM, XRD, and EDS collectively reveals the coexistence of the $CsPbBr_3$ and

MoS_2 phases, indicating the emergence of the $CsPbBr_3@MoS_2$ CS-NS.

The presence of MoS_2 sheets passivates all the $CsPbBr_3$ NCs, enhancing their stability and enabling dispersion in water or ethanol (EtOH). It is important to note that pure $CsPbBr_3$ NCs are unstable in polar solvents and decompose easily. Exceptionally, the synthesized $CsPbBr_3@MoS_2$ CS-NSs are stable in polar solvents, providing compelling evidence for the enhanced stability of the NCs. To assess the stability within polar solvents, we introduced the NCs and CS-NSs into an aqueous solution and closely observed the color changes (**Figure 1 f**). Significantly, the NCs underwent complete decomposition within a few minutes, marked by a change in color from yellowish to white. In contrast, the CS-NSs displayed remarkable resilience, remaining as they were without any decomposition in water for over a week, with the color persisting in a grayish hue.
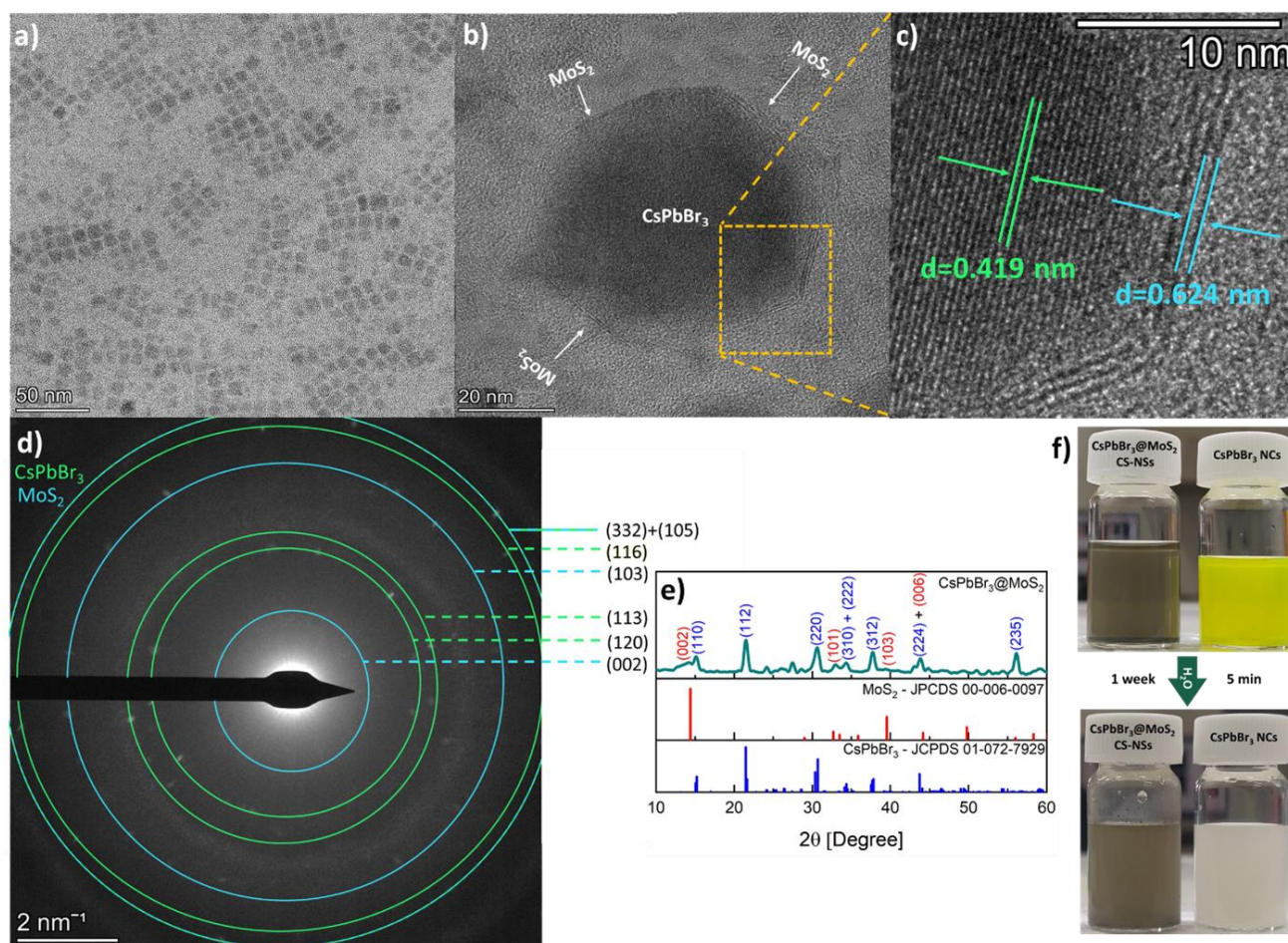

Figure 1. (a-c) TEM micrographs of (a) $CsPbBr_3$ NCs, (b) $CsPbBr_3@MoS_2$ CS-NS and (c) $CsPbBr_3@MoS_2$ CS-NS – the atomic lattice of the $CsPbBr_3$ with a lattice spacing of 0.419 nm (green), and MoS_2 with 0.624 nm (azure); (d) Diffraction rings of the CS-NSs, here the $CsPbBr_3$ and MoS_2 diffraction patterns are marked in green and azure, respectively; (e) XRD of the CS-NSs; (f) dispersion of $CsPbBr_3$ NCs and CS-NSs in toluene (on the top) and in water (on the bottom)

Optical Analysis

We employed optical analysis to support the TEM and XRD analysis findings. The absorption spectra of the $CsPbBr_3$ NCs and the CS-NSs are presented in **Figure 2 a**. The spectral analysis of $CsPbBr_3$ NCs exhibits a distinct cutoff at 512 nm, indicative of its

typical absorption edge (**Figure 2 a,** yellow line).[43] The PL spectra of the NCs exhibit a sharp emission peak at 509 nm with a high photoluminescence quantum yield (PLQY) of 92%, characteristic of the $CsPbBr_3$ NCs (**Figure 2 c,** yellow line).

3

Interestingly, upon forming CsPbBr$_3$@MoS$_2$, the absorption spectra display only MoS$_2$ peaks at 406, 613, and 665 nm, corresponding to the C, B, and A excitons, respectively (**Figure 2 a,** green line).[44] Moreover, the PL of the NCs is completely quenched **(Figure 2 c,** green line**).** This PL quenching and the absence of the absorbance peak of CsPbBr$_3$ signifies the complete formation of a MoS$_2$ sheath encapsulating the CsPbBr$_3$ NCs surface. The disappearance of the absorption edge of the NCs may stem from the variance in absorption coefficients between MoS$_2$ and CsPbBr$_3$. This observation is further supported by the simulated absorbance of the NCs and CS-NSs,

as discussed below. The PL quenching of the CsPbBr$_3$ NCs can be attributed to the charge or energy transfer from the conduction band (CB) of the NCs to the CB of MoS$_2$, which leads to the creation of an electron-hole pair.[35, 45] We calculated the NCs, MoS$_2$, and CS-NSs bandgaps using Tauc's plot. We found that the E$_g$ are ~2.38 eV, 1.83, and ~1.81 eV, corresponding to CsPbBr$_3$ and MoS$_2$, respectively (**Figures S11 a, e, f**).[3a, 46] The combination of findings obtained through XRD, TEM, PL, and absorption analyses thoroughly confirms the successful formation of the CS-NSs.
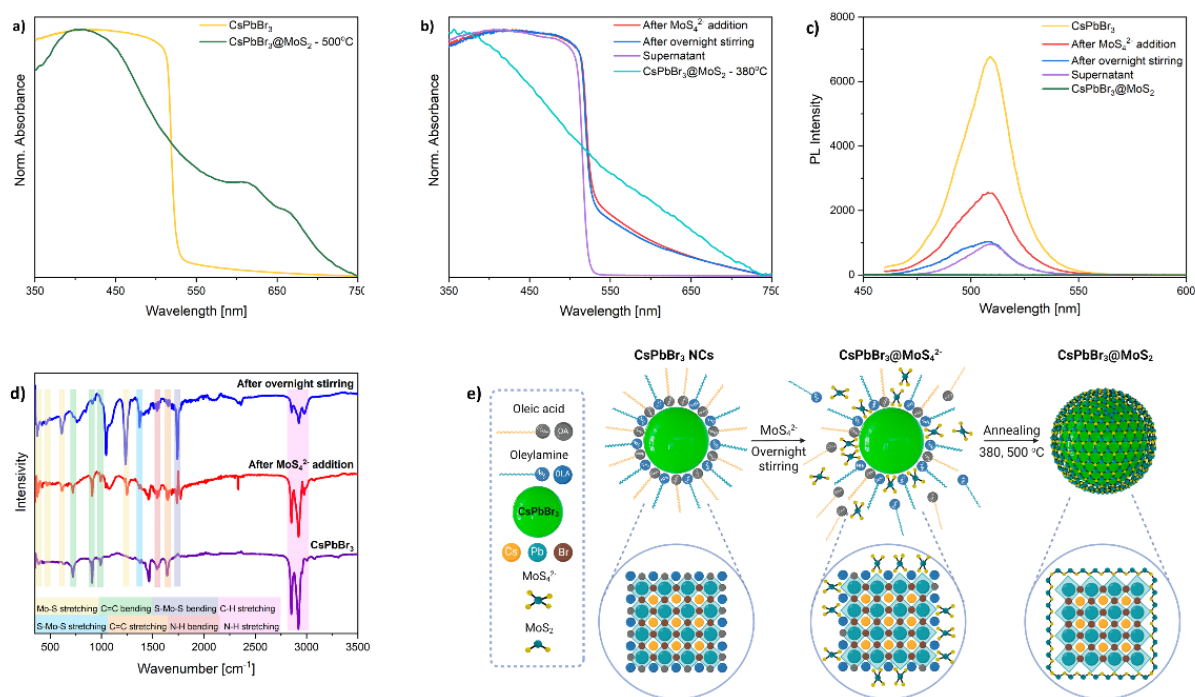

Figure 2. (a)-(b) UV-Vis absorbance spectra (c) PL spectra (d) FTIR of CsPbBr$_3$@MoS$_2$ CS-NSs at different synthesis stages and (e) the scheme of the reaction mechanism of the CS-NSs

Study of the Formation Mechanism of the CS-NSs Using Optoelectronic Properties

Here, we investigated the morphology and optical properties of the CS-NSs in order to understand their formation mechanism. To accomplish this objective, we assessed the optical characteristics at various stages of the synthetic process, encompassing absorbance, photoluminescence (PL), and Fourier-transform infrared (FTIR) spectroscopies. Despite its seeming simplicity in accomplishing the CsPbBr$_3$@MoS$_2$ nanostructure, we have encountered several significant difficulties through its synthesis. Hence, establishing the primary obstacles inherent in this notable and unexplored synthesis is imperative. The main challenges were (a) the high solubility of the CsPbBr$_3$ in polar solvents; (b) the precursor for MoS$_2$ formation, the (NH$_4$)$_2$MoS$_4$ salt, was insoluble in a non-polar solvent; (c) steric hindrance by the NCs ligands that prevent efficient MoS$_4^{2-}$ binding; (d) the melting temperature of the CsPbBr$_3$ NCs is below the MoS$_2$ crystallization temperature; and (e) formation of MoS$_2$ as a separate phase.

Solubility (challenge a and b)

Our initial focus was on selecting an appropriate solvent to facilitate the dissolution of the MoS$_2$ precursor, i.e., ammonium tetrathiomolybdate (ATTM or (NH$_4$)$_2$MoS$_4$), while preserving the structural integrity of CsPbBr$_3$ NCs. The procedure begins with the synthesis of CsPbBr$_3$ NCs [37], followed by overnight stirring with ATTM. A homogeneous mixture of CsPbBr$_3$ NCs and ATTM is crucial for the formation of CsPbBr$_3$@MoS$_4^{2-}$, which transforms into core-shell CsPbBr$_3$@MoS$_2$ CS-NSs during annealing. This step was challenging due to the orthogonal dispersion characteristics of NCs and ATTM. Namely, whereas CsPbBr$_3$ requires non-polar solvents for dispersion due to its lipophilic ligands, ATTM is soluble only in polar solvents owing to its ionic nature. Identifying a solvent that dissolves ATTM while maintaining the structural integrity of CsPbBr$_3$ is crucial. The most effective method to achieve that goal involves combining two miscible solvents with different polarities. Herein, we conducted dispersion and dissolution experiments using various solvents to determine the optimal solvent mixture. These solvents were classified according to their polarity. Subsequently, they were

4

analyzed based on their ability to dissolve ATTM and their impact on the structural and optical properties of $CsPbBr_3$ NCs (**Table S1**).

Furthermore, we undertook two concurrent analyses, exploring the dissolution and stability of $CsPbBr_3$ NCs and the solubility of the ATTM. We investigated these parameters in several chosen solvents, employing visual observations and measurements of absorbance and PL. The color change observed can be considered an indication of structural degradation.[47] The results of these measurements are shown in **Figures S8-10**. From the dissolution and stability study of NCs, we found that hexane and toluene were the most favorable solvents. In ethyl acetate (EtAc), the NCs exhibit stability for 10 minutes before initiating decomposition (**Figures S8 a, b**). This observation suggests that EtAc can serve as a secondary solvent with careful control over its concentration. The addition of EtAc will allow the enhancement of the polarity of the mixture without causing damage to the NCs. Our exploration of ATTM dissolution revealed that isopropyl alcohol (IPA), ethanol (EtOH), and EtAc demonstrate the capability to dissolve it. This consideration involved examining changes in the precipitation rates of the solute. Among these solvents, EtAc exhibited superior efficacy in dissolving ATTM (**Figure S10 a**). Moreover, as EtOH and IPA cause the dissolution of the NCs, EtAc stands out as the preferred additional solvent in the mixture. It effectively dissolves ATTM while being less detrimental to the structural integrity of $CsPbBr_3$, particularly when employed as a secondary solvent. Upon incorporating hexane as the primary solvent and reevaluating the solubility of ATTM, we observed that the most stable suspension was achieved with a mixture containing a 2:1 ratio of hexane to EtAc (v:v) (**Figure S10 b**). Indeed, we found that the 2:1 solvent mixture facilitates the dissolution of ATTM while preserving the structural integrity of $CsPbBr_3$ NCs. These findings guided CS-NSs synthesis, and the observed optical properties provided compelling evidence for the effectiveness of the hexane/ EtAc combination.

We employed optical analysis to investigate the growth mechanism, addressing concerns regarding the structural changes in NCs in the synthesis process. We initially stored the

Further, the PL study was employed to investigate the changes induced by the addition of ATTM. We found that the PL intensity (~509 nm) gradually decreases upon the addition of ATTM and further decays after overnight stirring (**Figure 2c**). Notably, immediately upon the addition of ATTM, the PL decreased by ~ 50%. The main reason is the dilution, as we introduce 5 mL of EtAc/ATTM to the 10 mL of hexane/NCs. Furthermore, a new peak emerges in the PL spectra at 485 nm following the addition of ATTM, and its intensity increases after the overnight stirring (**Figure 2 c, S13**, and **Table S3**). The appearance of an additional peak suggests a change in the aspect ratio of the NCs due to changes in ligand attachment.[49] To support this conclusion, we measured the PL spectra of the supernatant of the centrifuged $CsPbBr_3@MoS_4^{2-}$ after the overnight stirring. We expected that the bigger and heavier MoS_4^{2-} coated NCs would precipitate rapidly while unmodified NCs would remain in the supernatant. Indeed, the supernatant's spectra closely matched those of

pre-synthesized $CsPbBr_3$ in hexane and then added the $(NH_4)_2MoS_4$ dissolved in EtAc. The resulting blend was mixed overnight and subsequently centrifuged and annealed. To evaluate the survivability of the $CsPbBr_3$ NCs throughout the synthetic process, we measured their optical properties at each step of the synthesis: (I) after adding EtAc, (II) following overnight stirring, and (III) after centrifugation (**Figures 2 b, c**). In the first two steps (I, II), the NCs absorption remained consistent upon adding ATTM/EtAc. In the third step (III- centrifugation), the absorption and PL spectra of the supernatant containing residuals mirrored the original optical behavior of the NCs, confirming their integrity throughout these stages. Moreover, the bandgap value remained nearly unchanged at 2.35±0.03 eV throughout these steps (**Figures S11 a-d**). These findings indicate that we successfully developed a method for dissolving ATTM without destroying the $CsPbBr_3$ NCs.

Ligands exchange (Challenge c)
Upon investigating the changes induced by the addition of ATTM, we found an increase in absorbance spectra within the 520-800 nm region (**Figure 2 b**, red line). This rise might be rooted in several factors: (i) the presence of ions causing changes in the dielectric environment;[48] (ii) the contribution of the MoS_4^{2-} absorption; or (iii) the exchange between lipophilic ligands (oleic acid (OA) and oleylamine (OLAm)) and MoS_4^{2-} i.e., alterations in ligand binding.[11, 48] The latter is the most plausible, as the absorbance in the region 520-800 nm further increases after the overnight stirring (**Figure S12**). The repeated stirring–sonication cycle prevented aggregation of the ATTM and facilitated the exchange of tetrathiomolybdate ions with OA ligands. Furthermore, EtAc acts as a polarity enhancer, intensifying the affinity between the ligands and the solution. It decreases the density of ligands bound to the surface of NCs, thereby reducing the steric hindrance that impedes the efficient attachment of MoS_4^{2-}. Consequently, employing EtAc alongside the sonication/stirring cycles facilitated the formation of the $CsPbBr_3@MoS_4^{2-}$ core-shell structure.

uncoated NCs, with no significant peak at 485 nm. This relatively straightforward analysis strongly supports the inference that the ligand exchange process occurred, wherein MoS_4^{2-} replaced the OA and OLAm ligands. Furthermore, the successful separation of MoS_4^{2-}coated NCs from pristine $CsPbBr_3$ NCs was achieved through centrifugation, promoting the formation and a higher yield of CS-NSs.

FTIR spectroscopy can provide additional verification and a detailed demonstration of the ligand exchange. Here, we measured the $CsPbBr_3$ NCs in the hexane solution (**Figure 2 d**). The FTIR spectra of $CsPbBr_3$ NCs exhibit a characteristic spectrum, with peaks assigned to the ligands (OA and OLAm).[50] Upon addition of the ATTM to the $CsPbBr_3$ NCs solution, the FTIR spectra exhibited a few additional peaks located around 639, 470, and 372 cm^{-1}, which can be attributed to Mo-S stretching vibration (**Figure 2 d**, beige square).[51] We substantiate this assignment by juxtaposing the $CsPbBr_3$/ATTM IR spectra with that of the ATTM

5

precursor. (**Figure S14**). Also, the N-H stretching and bending peaks rise due to the additional amine in the ATTM solution (**Figure 2 d**, pink square). The intensity of the peaks assigned to C-H and N-H bending in the 3000-2800 cm^{-1} range decreased significantly due to diluting of the CsPbBr$_3$ NCs with the ATTM solution (**Figure 2 d**, pink square). Interestingly, following the introduction of the ATTM to the CsPbBr$_3$ solution, the intensity of the Mo-S peaks is weak and increases only after overnight stirring. These results strengthen our conclusion from the PL spectroscopy, indicating the exchange of ligands and the formation of MoS$_4^{2-}$ shell on top of the CsPbBr$_3$ NCs. Moreover, the intensity of the peaks associated with the ligands diminished significantly, suggesting that the ligands were partially removed from the surface of the CsPbBr$_3$ NCs. It is important to emphasize that the peaks that become apparent at 1075 and 1047 cm^{-1} are associated with the S=O stretching feature of sulfoxides originating from the ATTM precursor (**Figure S14**). Furthermore, we employ HAADF/EDS analysis to support our findings regarding the CsPbBr$_3$@MoS$_4^{2-}$ after the overnight stirring (**Figure S15**). The distribution regions of both the S and Br elements are identical, thereby providing supplementary confirmation regarding the attachment of MoS$_4^{2-}$ to the surface of the CsPbBr$_3$ NCs. Yet, the overlapping of Mo and S peaks prevented the attainment of an accurate ratio between them. In conclusion, a thorough analysis of the results obtained by FTIR spectroscopy and EDS demonstrates that the CsPbBr$_3$@MoS$_4^{2-}$ core-shell NPs are formed through ligand exchange (**Figure 2 e**).

Annealing and MoS$_2$ formation (challenge d and e)

The transformation from CsPbBr$_3$@MoS$_4^{2-}$ to core-shell CsPbBr$_3$@MoS$_2$ NSs was achieved by annealing the sample under a vacuum. During the annealing process, the MoS$_4^{2-}$ was reduced to MoS$_2$, releasing NH$_3$, S, and H$_2$S gases (**Equation S1**).[52] The product of the annealing process depends on the temperature gradient created in the reactor. The continuous pumping and the gradient allow vapor evacuation and modify the equilibrium such that excess sulfur can be released. The bending and close-cage formation of MoS$_2$ occurs due to the presence and chemical reactivity of dangling bonds.[52c, 53] This phenomenon facilitates the formation of CS-NSs.

As mentioned earlier, the formation of CS-NSs remains a highly challenging process, even after the successful formation of CsPbBr$_3$@MoS$_4^{2-}$. The crystallization of MoS$_2$ requires a high annealing temperature (~500 ℃), while the NCs melt at ~400 ℃ in a vacuum environment.[54] Indeed, the synthesis of MoS$_2$ can be activated at lower temperatures (~380 ℃), but a slightly higher temperature is necessary to produce a sufficient quantity of the substance. In addition, despite its low melting temperature, CsPbBr$_3$ can withstand temperatures of 500 ℃ during short-term annealing. A further complication in synthesizing the CS-NSs is the tendency of MoS$_2$ to form multilayer platelets as a separate bulk phase. To overcome this challenge, we implemented a rapid cooling technique. This technique successfully hindered the continuous growth of multiple layers of MoS$_2$ and maintained a thin layer of MoS$_2$ on top of the CsPbBr$_3$ NCs surface.[54-55] We chose a two-step annealing process to preserve the NCs and enable their encapsulation by MoS$_2$ sheets. The initial step in this

process involves swift (5 minutes) heating at 380 ℃, followed by immediate cessation through rapid cooling. Subsequently, the CsPbBr$_3$@MoS$_4^{2-}$ was heated to 500 ℃ for 10 minutes and cooled rapidly. Generally, upon heating, MoS$_4^{2-}$ (Mo^{VI}) would be reduced to form MoS$_2$ (Mo^{IV}).[52b] The fast heating allows partial reduction to MoS$_3$ and the formation of a small amount of MoS$_2$, which is apparent in the TEM image (**Figure S5 a-d**).[56] We hypothesize that this initial step promotes encapsulation of the CsPbBr$_3$ NCs. This prevents the NCs from melting during the second annealing step, as well as the formation of MoS$_2$ as a distinct phase. The rapid cooling helped maintain the closed cage structure of MoS$_2$, preventing the growth of additional layers (*challenge (e)*). TEM micrographs presented in **Figures S5 a-d** unveil the initial growth of MoS$_2$ during the first annealing process. After the second annealing step, the formation of the MoS$_2$ shell became significantly more apparent (**Figures 1 b, S6 a, b**). The XRD pattern from the initial annealing step displays faint MoS$_2$ peaks, suggesting insufficient crystallization of the layers (**Figure S5 e**). Following the second annealing step, the XRD pattern exhibits prominent MoS$_2$ peaks, underscoring the essential role of this step in facilitating the formation of MoS$_2$ sheets.

To decouple the contribution of the MoS$_2$ shell from the CsPbBr$_3$ core, we synthesized the pristine MoS$_2$ under synthetic conditions resembling those of CS-NSs (**Figure S12 b**). This strategy provided a solid foundation for comparing the optical properties of the CS-NSs to the pristine CsPbBr$_3$ and MoS$_2$. During the first annealing step, the distinctive spectral characteristics of CsPbBr$_3$ disappeared completely, and the spectra became distorted and somewhat lacking in distinct features (**Figure 2 b,** azure line). After the second annealing, the absorption spectra closely resembled that of pure MoS$_2$ (**Figure S12 b**).

Finite Difference Time Domain (FDTD) Simulations: Optical Absorbance and Electric Filed Distribution

We employed FDTD simulations to explore the optical behavior and identify the most favorable structure for achieving maximum absorption (the schematic of the simulation cross-section is presented in **Figure S17**). Specifically, we investigated the impact of varying the diameters of the CsPbBr$_3$ core (10 to 40 nm) and the number of MoS$_2$ layers (1 to 4 layers, 1L=0.615 nm)[46a, 57] on electric field intensity (|E^2|) and the absorbance spectra. We chose the diameter and number of MoS$_2$ layers based on the experimental results (**Figure S5**). The simulated and the experimental absorption spectra of MoS$_2$ and CsPbBr$_3$ are presented in **Figure 3 a**. The 520, 660, and 615 nm peaks in the absorption spectra correspond to the exciton of CsPbBr$_3$ and the A and B excitons of MoS$_2$, respectively.[57-58] The experimental and simulated data exhibit excellent overlap, indicating the accuracy of the simulation parameters.[57-58] In all simulations, the core sizes of CS-NSs did not significantly impact the absorbance of CsPbBr$_3$@MoS$_2$. The results consistently displayed features similar to those observed in experiments (**Figure S18**). Hence, a core radius of 40 nm produced the optimal intensity in the electric field and offered the potential for efficient light harvesting (**Figure S19**). Interestingly, the average core size in the synthesized CS-NS was found to be 33.86±1.2 nm. This finding further indicates

6

that 40 nm is an optimal choice for a core size of the $CsPbBr_3@MoS_2$ NC.

Figure 3 b shows the absorption spectra of $CsPbBr_3@MoS_2$ CS-NS with different numbers of MoS_2 layers (L). A remarkable enhancement (of x10) in the absorption intensity was observed upon adding a single MoS_2 layer to the $CsPbBr_3$ core. The absorption spectra of the $CsPbBr_3@4L-MoS_2$ exhibit similar features to their single-layer counterpart. However, there was a significant increase of two orders of magnitude in the absorption intensity at the 500-800 nm range between $CsPbBr_3@1L-MoS_2$ and $CsPbBr_3@4L-MoS_2$. Interestingly, the contribution from the $CsPbBr_3$ NC was almost undetectable due to the strong contribution from MoS_2. The high absorption coefficient of MoS_2 ($2.8 \cdot 10^6$ cm^{-1}) compared to $CsPbBr_3$ NC ($7.7 \cdot 10^4$ cm^{-1}) at a wavelength of 400 nm.[59] This difference can be the reason for the strong contribution of MoS_2 to the absorption of the CS-NS.[44,

and CS-NSs are presented in **Figures 3 c-f** and **S20**. A strong enhancement of E^2 upon adding MoS_2 layers corresponds to our previous observation regarding the enhancement in absorbance (**Figure 2 a**). The most pronounced E^2 enhancement can be found at λ=520 nm and 604 nm, where there is a major difference in the imaginary part of the dielectric function of $CsPbBr_3$ and MoS_2. Therefore, probing the E^2 at these specific wavelengths allows us to gain insights into the impact of the encapsulation. Interestingly, the E^2 enhancement was more conspicuous at λ=604 nm than at λ=520 nm. Moreover, we observed a 230% increase in the electric field for $CsPbBr_3@4L-MoS_2$ at λ=604 nm. The results showcase a substantial increase in E^2, surpassing the results of all previous studies by a significant margin.[60] At these wavelengths, the difference in ε_2 ($\Delta\varepsilon_2$) is 12.9 and 9.3 at λ=604 and 520 nm, respectively.[58a, 59b] The higher $\Delta\varepsilon_2$ at 604 nm induces a higher improvement in the electric field enhancement. Also, the ideal simulation environment may partly explain this
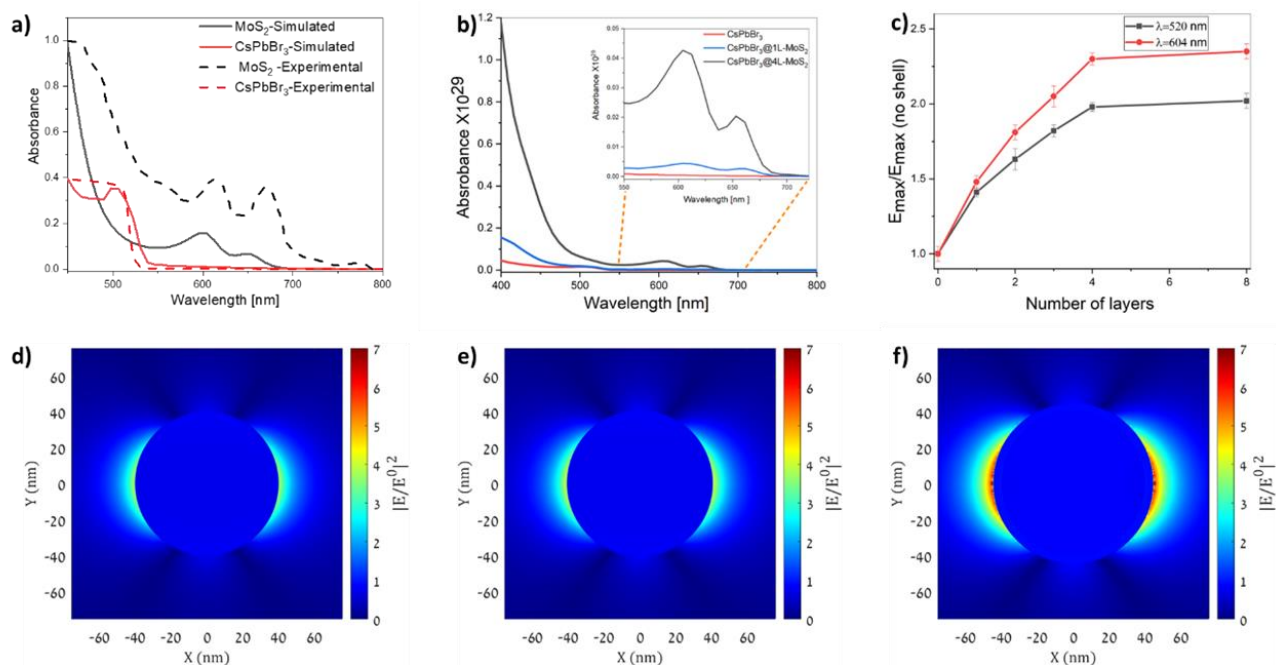
[59] The visualization of the electric field ($E^2 \approx |E/E^0|^2$) maps of NC

exceptional amplification in the electric field.

Figure 3. (a) Simulated and experimental absorbance spectra of $CsPbBr_3$ and MoS_2 (b) simulated absorbance spectra of $CsPbBr_3@MoS_2$ with the varied number of layers (c) Visualization of the electric field enhancement* of the $CsPbBr_3@MoS_2$ as a function of MoS_2 layers, for λ=604 nm and λ=520 nm and (d)-(f) Simulated electric field distribution of $CsPbBr_3@MoS_2$ at λ=604 nm (XY plane is perpendicular to the light source), (d) $CsPbBr_3$, (e) $CsPbBr_3@1L-MoS_2$, (f) $CsPbBr_3@4L-MoS_2$. (*E_{max} is defined as the local maximum absorption at wavelengths 520 and 604 nm for each number of layers

Indeed, both wavelengths exhibit a substantial E^2 enhancement. **Figure 3 c** illustrates a nonlinear increase in the E^2 intensity as the number of MoS_2 layers rises until the fourth layer; beyond this point, there is no notable impact. This is because the increase in shell size and the decrease in the area-to-volume ratio are interconnected, influencing the surface-related nonlinear response.[61] Hence, the observed behavior in the core-shell system can be attributed to factors such as charge transfer from the CB of $CsPbBr_3$ to the CB of MoS_2[62] or other nonlinear optical effects like multiphoton absorption.[63] This is because the increase in shell size and the decrease in the area-to-volume ratio are interconnected, influencing the surface-related nonlinear response.

Solar cell – Current density

After demonstrating considerable absorption enhancement, we simulated the short-circuit current (Jsc) of the solar cells. These simulations were done to evaluate the efficiency of CS-NS as an absorber. For this, we varied the volume percentage (% v/v) of the MoS_2 shell from 0% to 20%; here, 0% corresponds to pristine $CsPbBr_3$ and 20% to $CsPbBr_3@4L-MoS_2$ (**Eq. S7**). **Figure 4** presents the results of the simulated current density of the core-shell $CsPbBr_3@MoS_2$ as a function of the volume concentration of the MoS_2 shell.
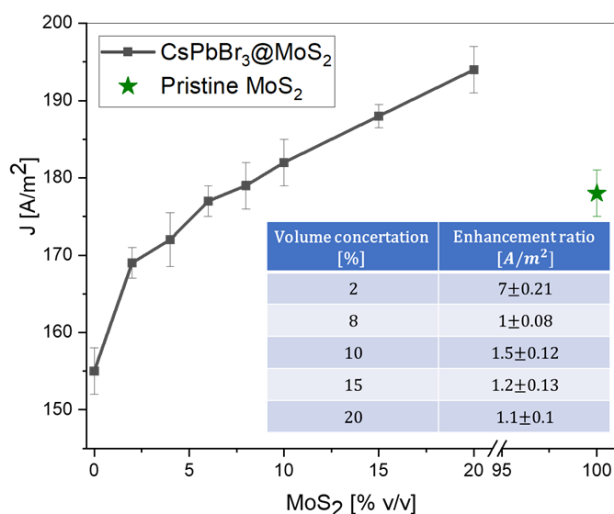
Figure 4. The current density of CsPbBr$_3$@MoS$_2$ core-shell solar cell with MoS$_2$ volume concentration (% v/v) and the enhancement ratio of Jsc*. The green star corresponds to the J$_{SC}$ of the pristine MoS$_2$ ‖ The *enhancement ratio of Jsc is defined as the curve slope between two points.

Volume concertation [%]	Enhancement ratio [A/m^2]
2	7±0.21
8	1±0.08
10	1.5±0.12
15	1.2±0.13
20	1.1±0.1

Figure 4 shows that an increase in the volume concentration of MoS$_2$ leads to an increase in the short circuit current of the cell-Jsc. The Jsc increases steadily with the edition of MoS$_2$, demonstrating that the latter significantly improves the CsPbBr$_3$@MoS$_2$-based solar cell devices. Moreover, the most substantial enhancement in Jsc reached 25.1%, occurring at 20% of MoS$_2$. Nonetheless, it is important to emphasize that the most significant enhancement ratio in the Jsc sample was achieved in the sample with 2v/v% MoS$_2$. The enhanced Jsc can be attributed to the greater absorbance of MoS$_2$. Moreover, there might be a synergetic effect, where MoS$_2$ serves as the hole conductor, whereas the CsPbBr$_3$ is an electron conductor. Thus, the core-shell structure promotes an efficient charge separation.[64] We noticed that the most significant enhancement ratio was between a pure CsPbBr$_3$ solar cell and a 2% (v/v) MoS$_2$ core-shell solar cell. The high absorption coefficient of MoS$_2$ makes it absorb a substantial amount of light even with only four layers; subsequently, a minimal amount of MoS$_2$ in solar cells can contribute to high device performance at a low cost.

Conclusion

In summary, we have successfully developed a novel synthetic approach for fabricating CsPbBr$_3$@MoS$_2$ core-shell nanostructures (CS-NSs) with promising applications in solar cells. The CS-NSs exhibit remarkable resilience, remaining intact in water for over a week. Structural and morphological analyses, including TEM, EDS, and XRD, validate the successful encapsulation of CsPbBr$_3$ by MoS$_2$. The CS-NSs showcase their exceptional potential for creating unique properties owing to the intimate interface formed through the complete coating and close attachment. Remarkably, the optical properties analysis reveals intriguing interactions between CsPbBr$_3$ and MoS$_2$, providing compelling evidence for the efficacy of the hexane/EtAc as a synthetic medium. Also, the PL spectra strongly support ligand exchange, which is crucial for successful core-shell formation

where MoS$_4^{2-}$ replaces OA and OLAm ligands, affirmed by successful separation through centrifugation. The theoretical FDTD simulations also show enhanced responses with an optimal MoS$_2$ thickness of 4 layers. Significant electric field enhancement (up to 230%) upon introducing MoS$_2$ layers indicates potential for improved light absorption and exciton generation. This research paves the way for stable, non-toxic hybrid perovskites beneficial for solar cells, photocatalysis, and other applications. The findings underscore the potential of CsPbBr$_3$@MoS$_2$ for converting solar energy, producing renewable energy, and serving as a clean source of electricity.

Acknowledgment

Supporting Information

The authors have cited additional references within the Supporting Information.[37b, 52a, 57-58, 65]

Keywords: Halide perovskites • CsPbBr$_3$@MoS$_2$ core-shell • Perovskite solar cells • Nanoparticles

References

[1] P. J. Megía, A. J. Vizcaíno, J. A. Calles, A. Carrero, *Energy & Fuels* **2021**, *35*, 16403-16415.

[2] H. Huang, M. I. Bodnarchuk, S. V. Kershaw, M. V. Kovalenko, A. L. Rogach, *ACS Energy Lett* **2017**, *2*, 2071-2083.

[3] **a)** Q. A. Akkerman, V. D'Innocenzo, S. Accornero, A. Scarpellini, A. Petrozza, M. Prato, L. Manna, *J Am Chem Soc* **2015**, *137*, 10276-10281; **b)** G. E. Eperon, T. Leijtens, K. A. Bush, R. Prasanna, T. Green, J. T. W. Wang, D. P. McMeekin, G. Volonakis, R. L. Milot, R. May, A. Palmstrom, D. J. Slotcavage, R. A. Belisle, J. B. Patel, E. S. Parrott, R. J. Sutton, W. Ma, F. Moghadam, B. Conings, A. Babayigit, H. G. Boyen, S. Bent, F. Giustino, L. M. Herz, M. B. Johnston, M. D. McGehee, H. J. Snaith, *Science* **2016**, *354*, 861-865; **c)** H. Tsai, W. Nie, J. C. Blancon, C. C. Stoumpos, R. Asadpour, B. Harutyunyan, A. J. Neukirch, R. Verduzco, J. J. Crochet, S. Tretiak, L. Pedesseau, J. Even, M. A. Alam, G. Gupta, J. Lou, P. M. Ajayan, M. J. Bedzyk, M. G. Kanatzidis, *Nature* **2016**, *536*, 312-316; **d)** Y. Wang, X. Li, V. Nalla, H. Zeng, H. Sun, *Adv Funct Mater* **2017**, *27*, 1605088.

[4] J. Li, L. Xu, T. Wang, J. Song, J. Chen, J. Xue, Y. Dong, B. Cai, Q. Shan, B. Han, H. Zeng, *Adv Mater* **2017**, *29*.

[5] **a)** Z. Liu, J. Yang, J. Du, Z. Hu, T. Shi, Z. Zhang, Y. Liu, X. Tang, Y. Leng, R. Li, *ACS Nano* **2018**, *12*, 5923-5931; **b)** S. Yakunin, L. Protesescu, F. Krieg, M. I. Bodnarchuk, G. Nedelcu, M. Humer, G. De Luca, M. Fiebig, W. Heiss, M. V. Kovalenko, *Nat. Commun* **2015**, *6*, 8056.

[6] **a)** M. V. Kovalenko, L. Protesescu, M. I. Bodnarchuk, *Science* **2017**, *358*, 745–750; **b)** P. Ramasamy, D. H. Lim, B. Kim, S. H. Lee, M. S. Lee, J. S. Lee, *Chem Commun (Camb)* **2016**, *52*, 2067-2070.

[7] X. Zhao, S. Chen, H. Yin, S. Jiang, K. Zhao, J. Kang, P. F. Liu, L. Jiang, Z. Zhu, D. Cui, P. Liu, X. Han, H. G. Yang, H. Zhao, *Matter* **2020**, *3*, 935-949.

[8] **a)** J. Kang, L. W. Wang, *J Phys Chem Lett* **2017**, *8*, 489-493; **b)** A. Swarnkar, R. Chulliyil, V. K. Ravi, M. Irfanullah, A. Chowdhury, A. Nag, *Angew. Chem.* **2015**, *127*, 15644-15648.

[9] B. Zhang, L. Goldoni, C. Lambruschini, L. Moni, M. Imran, A. Pianetti, V. Pinchetti, S. Brovelli, L. De Trizio, L. Manna, *Nano Lett* **2020**, *20*, 8847-8853.

[10] C. Otero-Martinez, N. Fiuza-Maneiro, L. Polavarapu, *ACS Appl Mater Interfaces* **2022**, *14*, 34291-34302.

[11] J. De Roo, M. Ibanez, P. Geiregat, G. Nedelcu, W. Walravens, J. Maes, J. C. Martins, I. Van Driessche, M. V. Kovalenko, Z. Hens, *ACS Nano* **2016**, *10*, 2071-2081.

8

[12] B. Luo, Y. C. Pu, S. A. Lindley, Y. Yang, L. Lu, Y. Li, X. Li, J. Z. Zhang, *Angew. Chem. Int. Ed.* **2016**, *55*, 8864-8868.

[13] B. Peng, J. Li, Q. Li, Y. Li, H. Zhu, L. Zhang, X. Wang, L. Bi, H. Lu, J. Xie, L. Deng, Q. Xu, K. Loh, *RSC Advances* **2017**, *7*, 18366-18373.

[14] G. H. Ahmed, J. Yin, O. M. Bakr, O. F. Mohammed, *ACS Energy Lett* **2021**, *6*, 1340-1357.

[15] P. N. Immanuel, S. J. Huang, V. Danchuk, A. Sedova, J. Prilusky, A. Goldreich, H. Shalom, A. Musin, L. Yadgarov, *Nanomaterials* **2022**, *12*.

[16] **a)** Y. Huang, F. Li, L. Qiu, F. Lin, Z. Lai, S. Wang, L. Lin, Y. Zhu, Y. Wang, Y. Jiang, X. Chen, *ACS Appl Mater Interfaces* **2019**, *11*, 26384-26391; **b)** A. Loiudice, S. Saris, E. Oveisi, D. T. L. Alexander, R. Buonsanti, *Angew Chem Int Ed Engl* **2017**, *56*, 10696-10701; **c)** X. Tang, W. Chen, Z. Liu, J. Du, Z. Yao, Y. Huang, C. Chen, Z. Yang, T. Shi, W. Hu, Z. Zang, Y. Chen, Y. Leng, *Small* **2019**, *15*, e1900484.

[17] **a)** Q. Xiang, B. Zhou, K. Cao, Y. Wen, Y. Li, Z. Wang, C. Jiang, B. Shan, R. Chen, *Chem Mater* **2018**, *30*, 8486-8494; **b)** Q. Zhong, M. Cao, H. Hu, D. Yang, M. Chen, P. Li, L. Wu, Q. Zhang, *ACS Nano* **2018**, *12*, 8579-8587.

[18] C. Sun, Y. Zhang, C. Ruan, C. Yin, X. Wang, Y. Wang, W. W. Yu, *Adv Mater* **2016**, *28*, 10088-10094.

[19] **a)** X. Liu, X. Zhang, L. Li, J. Xu, S. Yu, X. Gong, J. Zhang, H. Yin, *ACS Appl Mater Interfaces* **2019**, *11*, 40923-40931; **b)** X. Zhang, M. Lu, Y. Zhang, H. Wu, X. Shen, W. Zhang, W. Zheng, V. L. Colvin, W. W. Yu, *ACS Cent Sci* **2018**, *4*, 1352-1359.

[20] **a)** W. Chen, T. Shi, J. Du, Z. Zang, Z. Yao, M. Li, K. Sun, W. Hu, Y. Leng, X. Tang, *ACS Appl Mater Interfaces* **2018**, *10*, 43978-43986; **b)** V. K. Ravi, S. Saikia, S. Yadav, V. V. Nawale, A. Nag, *ACS Energy Lett* **2020**, *5*, 1794-1796.

[21] A. Dey, J. Ye, A. De, E. Debroye, S. K. Ha, E. Bladt, A. S. Kshirsagar, Z. Wang, J. Yin, Y. Wang, L. N. Quan, F. Yan, M. Gao, X. Li, J. Shamsi, T. Debnath, M. Cao, M. A. Scheel, S. Kumar, J. A. Steele, M. Gerhard, L. Chouhan, K. Xu, X. G. Wu, Y. Li, Y. Zhang, A. Dutta, C. Han, I. Vincon, A. L. Rogach, A. Nag, A. Samanta, B. A. Korgel, C. J. Shih, D. R. Gamelin, D. H. Son, H. Zeng, H. Zhong, H. Sun, H. V. Demir, I. G. Scheblykin, I. Mora-Sero, J. K. Stolarczyk, J. Z. Zhang, J. Feldmann, J. Hofkens, J. M. Luther, J. Perez-Prieto, L. Li, L. Manna, M. I. Bodnarchuk, M. V. Kovalenko, M. B. J. Roeffaers, N. Pradhan, O. F. Mohammed, O. M. Bakr, P. Yang, P. Muller-Buschbaum, P. V. Kamat, Q. Bao, Q. Zhang, R. Krahne, R. E. Galian, S. D. Stranks, S. Bals, V. Biju, W. A. Tisdale, Y. Yan, R. L. Z. Hoye, L. Polavarapu, *ACS Nano* **2021**, *15*, 10775-10981.

[22] R. Marks, A. Schranck, R. Stillwellb, K. Doudrick, *RSC Adv.*, **2020**, , *10*, .

[23] **a)** W. Chen, J. Hao, W. Hu, Z. Zang, X. Tang, L. Fang, T. Niu, M. Zhou, *Small* **2017**, *13*, 1604085; **b)** Y. Tang, X. Cao, Q. Chi, in *Two-dimensional Materials for Photodetector*, **2018**.

[24] **a)** C. H. Ravikumar, G. V. Nair, S. Muralikrishna, D. H. Nagaraju, R. G. Balakrishna, *Mater Lett* **2018**, *220*, 133-135; **b)** C. Ruffman, C. K. Gordon, E. Skúlason, A. L. Garden, *J Phys Chem C Nanomater Interfaces* **2020**, *124*, 17015-17026; **c)** S. Rubtsov, A. Musin, V. Danchuk, M. Shatalov, N. Prasad, M. Zinigrad, L. Yadgarov, *Nanomaterials* **2023**, *13*, 2675.

[25] T. F. Jaramillo, K. P. Jorgensen, J. Bonde, J. H. Nielsen, S. Horch, I. Chorkendorff, *Science* **2007**, *317*, 100-102.

[26] S. S. Chou, B. Kaehr, J. Kim, B. M. Foley, M. De, P. E. Hopkins, J. Huang, C. J. Brinker, V. P. Dravid, *Angew Chem Int Ed Engl* **2013**, *52*, 4160-4164.

[27] **a)** C. A. Papageorgopoulos, W. J. l, *Surf Sci* **1995**, *338* 83-93; **b)** F. S. Ohuchi, W . Jaegermann, J. J C. Pettenkofer, B. A. Parkinson, *Langmuir* **1989**, *5*, 439-442; **c)** J. L. Stickney, S. D. Rosasco, B. C. Schardt, T. Solomun, A. T. Hubbard, B. A. Parkinson, *Surf Sci* **1984**, *136*, 15-22; **d)** B. A. Parkinson, *J. Am. Chem. Soc.* **1990**, 1030-1033.

[28] Y. Lin, B. Adilbekova, Y. Firdaus, E. Yengel, H. Faber, M. Sajjad, X. Zheng, E. Yarali, A. Seitkhan, O. M. Bakr, A. El-Labban, U. Schwingenschlogl, V. Tung, I. McCulloch, F. Laquai, T. D. Anthopoulos, *Adv Mater* **2019**, *31*, e1902965.

[29] D. J. Late, Y. K. Huang, B. Liu, J. Acharya, S. N. Shirodkar, J. Luo, A. Yan, D. Charles, U. V. Waghmare, V. P. Dravid, C. N. Rao, *ACS Nano* **2013**, *7*, 4879-4891.

[30] E. J. Juarez-Perez, M. Wubetaler, F. Fabregat-Santiago, K. Lakus-Wollny, E. Mankel, T. Mayer, W. Jaegermann, I. Mora-Sero, *J Phys Chem Lett* **2014**, *5*, 680-685.

[31] **a)** N. Sariff, Z. H. Ismail, A. S. H. M. Yasir, D. Sooriamoorthy, P. N. A. F. S. Mahadzir, in *Motion Planning for Dynamic Agents*, IntechOpen, **2023**; **b)** M. Karimipour, S. Khazraei, B. Jo Kim, G. Boschloo, E. M. J. Johansson, *ACS Appl. Energy Mater.* **2021**, , *4*, 14080–14092.

[32] **a)** Z. Liu, K. Liu, F. Zhang, S. M. Jain, T. He, Y. Jiang, P. Liu, J. Yang, H. Liu, M. Yuan, *Sol Energy* **2020**, *195*, 436-445; **b)** R. Long, O. V. Prezhdo, *ACS Nano* **2015**, *9*, 11143-11155.

[33] **a)** J. Ghosh, P. K. Giri, *JPhys Materials* **2021**, *4*, 032008; **b)** T. F. Hongmei Ju , Yun Zhou , Xianbin Feng, Tinghui Song , Feng Lu, Wenchao Liu, *Appl Surf Sci* **2021**, *551*.

[34] **a)** S. R. Tamalampudi, J.-Y. Lu, N. Rajput, C.-Y. Lai, B. Alfakes, R. Sankar, H. Apostoleris, S. P. Patole, I. Almansouri, M. Chiesa, *npj 2D mater. appl.* **2020**, *4*, 23; **b)** S. Vaidya, A. K. Ganguli, in *Comprehensive Nanoscience and Nanotechnology*, **2019**, pp. 1-12.

[35] X. Song, X. Liu, D. Yu, C. Huo, J. Ji, X. Li, S. Zhang, Y. Zou, G. Zhu, Y. Wang, M. Wu, A. Xie, H. Zeng, *ACS Appl Mater Interfaces* **2018**, *10*, 2801-2809.

[36] D. Xie, L. Wei, M. Xie, L. Jiang, J. Yang, J. He, J. Jiang, *Adv Funct Mater* **2021**, *31*, 2010655.

[37] **a)** T. Udayabhaskararao, L. Houben, H. Cohen, M. Menahem, I. Pinkas, L. Avram, T. Wolf, A. Teitelboim, M. Leskes, O. Yaffe, D. Oron, M. Kazes, *Chem Mater* **2017**, *30*, 84-93; **b)** L. Protesescu, S. Yakunin, M. I. Bodnarchuk, F. Krieg, R. Caputo, C. H. Hendon, R. X. Yang, A. Walsh, M. V. Kovalenko, *Nano letters* **2015**, *15*, 3692-3696.

[38] J. Kim, L. Hu, H. Chen, X. Guan, P. R. Anandan, F. Li, J. Tang, C.-H. Lin, K. Kalantar-Zadeh, A. Tricoli, T. Wu, *ACS Mater Lett* **2020**, *2*, 1368-1374.

[39] R. Dai, A. Zhang, Z. Pan, A. M. Al-Enizi, A. A. Elzatahry, L. Hu, G. Zheng, *Small* **2016**, *12*, 2792-2799.

[40] **a)** Y. He, L. Matei, H. J. Jung, K. M. McCall, M. Chen, C. C. Stoumpos, Z. Liu, J. A. Peters, D. Y. Chung, B. W. Wessels, M. R. Wasielewski, V. P. Dravid, A. Burger, M. G. Kanatzidis, *Nat Commun* **2018**, *9*, 1609; **b)** C. C. Stoumpos, C. D. Malliakas, J. A. Peters, Z. Liu, M. Sebastian, J. Im, T. C. Chasapis, A. C. Wibowo, D. Y. Chung, A. J. Freeman, B. W. Wessels, M. G. Kanatzidis, *Cryst. Growth Des* **2013**, *13*, 2722-2727.

[41] A. Zak, Y. Feldman, V. Lyakhovitskaya, G. Leitus, R. Popovitz-Biro, E. Wachtel, H. Cohen, S. Reich, R. Tenne, *J. Am. Chem. Soc.* **2002**, *12*, 4747-4758.

[42] **a)** D. E. Newbury, N. W. Ritchie, *J Mater Sci* **2015**, *50*, 493-518; **b)** L. Rapoport, A. Moshkovich, V. Perfilyev, A. Laikhtman, I. Lapsker, L. Yadgarov, R. Rosentsveig, R. Tenne, *Tribol Lett* **2011**, *45*, 257-264.

[43] L. Rao, X. Ding, X. Du, G. Liang, Y. Tang, K. Tang, J. Z. Zhang, *Beilstein Journal of Nanotechnology* **2019**, *10*, 666-676.

[44] I. A. Rahman, A. Purqon, *J Phys Conf Ser* **2017**, *877*, 012026.

[45] **a)** J. Ghosh, L. P. L. Mawlong, M. G. B, A. J. Pattison, W. Theis, S. Chakraborty, P. K. Giri, *J Mater Chem C Mater* **2020**, *8*, 8917-8934; **b)** X. Wang, J. He, K. Li, Y. Mao, X. Cai, C. Sun, M. Zhu, *Chem Eng J* **2021**, *416*, 128077.

[46] **a)** E. Scalise, M. Houssa, G. Pourtois, V. V. Afanas'ev, A. Stesmans, *Physica E Low Dimens Syst Nanostruct* **2014**, *56*, 416-421; **b)** C. Zhang, A. Johnson, C. L. Hsu, L. J. Li, C. K. Shih, *Nano Lett* **2014**, *14*, 2443-2447.

[47] S. Huang, Z. Li, B. Wang, N. Zhu, C. Zhang, L. Kong, Q. Zhang, A. Shan, L. Li, *ACS Appl Mater Interfaces* **2017**, *9*, 7249-7258.

[48] Y. Murakami, S. Maruyama, *Phys Rev B* **2009**, *79*, 155445.

[49] **a)** S. A. Veldhuis, Y. F. Ng, R. Ahmad, A. Bruno, N. F. Jamaludin, B. Damodaran, N. Mathews, S. G. Mhaisalkar, *ACS Energy Lett* **2018**, *3*, 526-531; **b)** Q. Zhang, S.-J. Liu, S.-H. Yu, *J. Mater. Chem.* **2009**, *19*, 191-207.

[50] N. K. Kumawat, X. K. Liu, D. Kabra, F. Gao, *Nanoscale* **2019**, *11*, 2109-2120.

[51] F. Maugéa, J. Lamotte, N. S. Nesterenko, O. Manoilova, A. A. Tsyganenko, *Catal Today* **2001**, *70* 271–284.

[52] **a)** H. W. Wang, P. Skeldon, G. E. Thompson, *J Mater Sci* **1998**, *33*, 3079-3083; **b)** A. Lavie, L. Yadgarov, L. Houben, R. Popovitz-Biro, T. E. Shaul, A. Nagler, H. Suchowski, R. Tenne, *Nanotechnology* **2017**, *28*, 24LT03; **c)** R. Tenne, *Chem. Eur. J.* **2002**, *8*, 5296-5304.

[53] V. Kundrat, Z. Kral, I. Pinkas, J. Pinkas, L. Yadgarov, *Ceram Int* **2024**, *50*, 7314-7322.

[54] **a)** M. Liao, B. Shan, M. Li, *J. Phys. Chem. Lett.* **2019**, *10*, 1217-1225; **b)** C. Zhang, J. F. S. Fernando, K. L. Firestein, J. E. von Treifeldt, D. Siriwardena, X. Fang, D. Golberg, *APL Materials* **2019**, *7*, 071110.

[55] R. Kreizman, A. N. Enyashin, F. L. Deepak, A. Albu-Yaron, R. Popovitz-Biro, G. Seifert, R. Tenne, *Adv Funct Mater* **2010**, *20*, 2459-2468.

[56] **a)** K. S. Liang, S. P. Cramer, D. C. Johnston, C. H. Chang, A. J. Jacobson, J. P. Deneufville, R. R. Chianelli, *J. Non-Cryst. Solids* **1980**, *42*, 345-356; **b)** T. Weber, J. C. Muijsers, J. W. Niemantsverdriet, *J. Phys. Chem.* **1995**, *99*, 9194-9200.

[57] Y. Li, A. Chernikov, X. Zhang, A. Rigosi, H. M. Hill, A. M. Van Der Zande, D. A. Chenet, E.-M. Shih, J. Hone, T. F. Heinz, *Phys Rev B* **2014**, *90*, 205422.

[58] **a)** G. Mannino, l. Deretzis, E. Smecca, A. La Magna, A. Alberti, D. Ceratti, D. Cahen, *J. Phys. Chem. Lett.* **2020**, *11*, 2490-2496; **b)** I. A. Rahman, A. Purqon, in *J Phys Conf Ser, Vol. 877*, IOP Publishing, **2017**, p. 012026.

[59] **a)** J. Y. Kwak, *Results Phys* **2019**, *13*, 102202; **b)** J. Maes, L. Balcaen, E. Drijvers, Q. Zhao, J. De Roo, A. Vantomme, F. Vanhaecke, P. Geiregat, Z. Hens, *J. Phys. Chem. Lett.* **2018**, *9*, 3093-3097.

[60] S. B. Kalkan, E. Najafidehaghani, Z. Gan, J. Drewniok, M. F. Lichtenegger, U. Hübner, A. S. Urban, A. George, A. Turchanin, B. Nickel, *Adv Opt Mater* **2022**, *11*.

[61] U. E. Kalsoom, R. Yi, J. Qu, L. Liu, *Front Phys* **2021**, *9*, 612070.

[62] Y. Li, N. Dong, S. Zhang, X. Zhang, Y. Feng, K. Wang, L. Zhang, J. Wang, *Laser Photon Rev* **2015**, *9*, 427-434.

[63] R. Sa, D. Liu, Y. Chen, S. Ying, *ACS Omega* **2020**, *5*, 4347-4351.

[64] M. I. Saidaminov, M. A. Haque, J. Almutlaq, S. Sarmah, X. H. Miao, R. Begum, A. A. Zhumekenov, I. Dursun, N. Cho, B. Murali, O. F. Mohammed, T. Wu, O. M. Bakr, *Adv Opt Mater* **2016**, *5*.

[65] **a)** Y. Bai, M. Hao, S. Ding, P. Chen, L. Wang, *Adv Mater* **2022**, *34*, 2105958; **b)** A. Bar-Hen, R. Bar-Ziv, T. Ohaion-Raz, A. Mizrahi, S. Hettler, R. Arenal, M. B. Sadan, *Chem Eng J* **2021**, *420*, 129771; **c)** J. De Roo, R. Ibáñez, P. Geiregat, G. Nedelcu, W. Walravens, J. Maes, J. C. Martins, I. Van Driessche, M. V. Kovalenko, Z. Hens, *ACS Nano* **2016**, *10*, 2071-2081; **d)** X. Fan, D. J. Singh, W. Zheng, *J. Phys. Chem. Lett.* **2016**, *7*, 2175-2181; **e)** P. B. Johnson, R.-W. Christy, *Phys Rev B* **1972**, *6*, 4370; **f)** A. Lavie, L. Yadgarov,

9

L. Houben, R. Popovitz-Biro, T.-E. Shaul, A. Nagler, H. Suchowski, R. Tenne, *Nanotechnology* **2017**, *28*, 24LT03; **g**) J. I. Pankove, *Optical processes in semiconductors*, Courier Corporation, **1975**; **h**) T. Udayabhaskararao, L. Houben, H. Cohen, M. Menahem, I. Pinkas, L. Avram, T. Wolf, A. Teitelboim, M. Leskes, O. Yaffe, D. Oron, M. Kazes, *Chem Mater* **2018**, *30*, 84-93; **i**) T. Welton, C. Reichardt, *Solvents and solvent effects in organic chemistry*, John Wiley & Sons, **2011**; **j**) F. X. Xiao, B. Liu, *Adv. Mater. Interfaces* **2018**, *5*, 1701098; **k**) C. Zhang, Q. Qian, L. Qin, X. Zhu, C. Wang, X. Li, *ACS Photonics* **2018**, *5*, 5079-5085.

10

11